Scanning Eye-Safe Elastic Backscatter Lidar at 1.54 μm

SCOTT M. SPULER AND SHANE D. MAYOR

National Center for Atmospheric Research, Boulder, Colorado

ABSTRACT

A field-deployable scanning direct-detection elastic backscatter lidar system that is eye safe at all ranges is presented. The first two-dimensional spatial images created by scanning this new 1.54-μm wavelength system, and time-lapse animations (viewable in the online version of this article) of those spatial images, are shown. The system has a useful range from approximately 500 m to several kilometers or more (depending on weather conditions) with 3-m range resolution. The time-lapse animations reveal the advection of the macroscopic structure of aerosol scattering due to atmospheric motion. The images and animations are ideal for the location of sources of pollutants and their dispersal and the elucidation of structure in the cloud-free atmosphere. Most importantly, the data presented were collected in a populated area, which would have not been possible with a non-eye-safe system.

1. Introduction

This paper presents the first results from a fieldable new lidar system that has the following features: pulse energy in excess of 170 mJ at 10 Hz, eye safety at all ranges, backscatter range resolution of 3 m, and full-hemispheric scanning. The details of the transmitter and receiver are described in Mayor and Spuler (2004, hereafter MS). However, since that publication the system has been transformed from a proof-of-concept laboratory experiment to a field-deployable instrument. Herein we discuss the many advancements and improvements over the laboratory prototype. These include a custom high-optical-efficiency receiving telescope, improved focusing lens, high-bandwidth photodetector/amplifier module, improved laser polarization, a custom 40-cm clear-aperture elevation over azimuth beam-steering unit (BSU) to facilitate scanning, and custom software for real-time visualization of scanning data. We refer to the system as the Raman-Shifted Eye-Safe Aerosol Lidar (REAL).

REAL builds on the volume imaging lidar (VIL) concept pioneered by Eloranta and coworkers at the University of Wisconsin (UW; Eloranta et al. 1975;

Kunkel et al. 1977). The full potential of the UW-VIL for visualizing atmospheric structure, monitoring boundary layer depth, mapping vector wind fields, etc., is restricted due its ocular hazard. The milestone we present here is a scanning analog direct-detection lidar that achieves approximately 50% of the pulse energy of the UW-VIL and yet is eye safe at all ranges. This is made possible by operating at the presently challenging wavelength of 1.54 μm (the UW-VIL operates at 1.06 μm). Therefore, REAL can be used in urban areas or during field experiments where research aircraft may fly through the lidar beam. We note that the UW-VIL features an average transmit power of 40 W (400 mJ per pulse at 100 Hz) and REAL currently transmits less than 2-W average power (170 mJ per pulse at 10 Hz). Fortunately, the 1.5-μm-wavelength region allows for safe transmission of even higher energy pulses. We recently achieved over 37% conversion efficiency generating 1.54 μm in our laboratory. Therefore, we are optimistic that lidars with UW-VIL power and performance can be made eye safe in the near future by operating at this wavelength.

2. Principles of operation

In summary, REAL is unique in that it successfully operates with high pulse energy at 1.54-μm wavelength. Within the wavelength range of 0.2–10 μm the highest maximum permissible exposure (MPE) for the human

Corresponding author address: Dr. Scott M. Spuler, National Center for Atmospheric Research, P.O. Box 3000, Boulder, CO 80307-3000.
E-mail: spuler@ucar.edu

eye is between 1.5 and 1.8 μm (Laser Institute of America 2000). Because of the large MPE in this spectral region, one can safely transmit very energetic pulses and employ analog detection to collect a high signal-to-noise ratio backscatter return from each shot. When extended to pulse repetition frequencies of at least 10 Hz, the angular resolution becomes sufficient to create scans. Operation at this wavelength for aerosol backscatter has additional advantages, including low molecular scattering, lack of atmospheric species absorption, and low sky background. Other lidars, such as coherent Doppler lidars in the infrared or micropulse lidars in the visible, are typically also eye safe but do not feature the 3-m range resolution or provide aerosol backscatter with such high signal to noise as an analog detection system. A general system schematic of REAL is included as Fig. 1.

a. Transmitter

REAL employs a commercially available flash-lamp-pumped Nd:YAG laser capable of generating 800 mJ per pulse at 10 Hz with a pulse length of 6 ns. The polarization purity of the laser is improved by placing a thin film plate polarizer at the exit of the laser albeit with a reduction of energy to ~615 mJ per pulse. The improved polarization allows for the provision of optical isolation to the pump laser and is a first step toward future depolarization measurements. The fundamental wavelength of the laser is converted to 1.543 μm via stimulated Raman scattering with >30% efficiency in a high pressure cell filled with pure CH_4 at 8–12 atmospheres of pressure. The Raman cell transmitter is unique in that it employs a nonfocused pump beam with multipass geometry, internal fans, and a diode injection seed at the Stokes wavelength. The design overcomes the severe limitations of previous methane cell-based transmitters, such as poor beam quality and production of carbon soot, which limited operational lifetime. A more detailed description of the frequency converter can be found in MS. After the conversion process the non-eye-safe pump beam is spatially separated by a high-dispersion prism and removed so that only the eye-safe beam is transmitted into the atmosphere. The transmitted pulses are approximately 4 ns in duration with a half-angle divergence of ~0.2 mrad.

b. Receiver

The system uses a 40.6-cm (16 in.) diameter telescope to collect backscattered light from the atmosphere. The commercial telescope (f/10 Schmidt-Cassegrain) described in MS was replaced with an f/3 Newtonian design for this work. The new telescope features a smaller
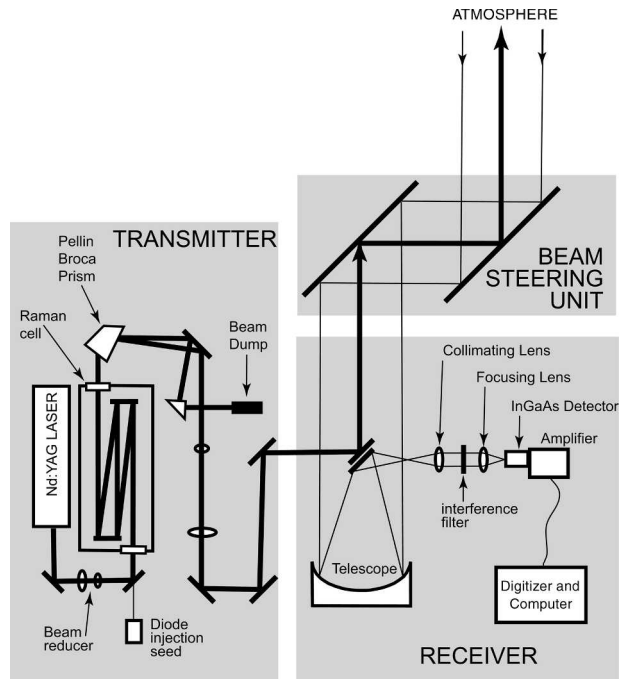

FIG. 1. General system schematic of REAL.

obscuration and gold-coated optics for improved reflectivity at 1.5-μm wavelength. These two features boost the effective transmission to 90% compared to the commercial telescope, which only had 67% transmission. A turning mirror mounted on the backside of the telescope secondary is used to direct the transmitted beam into the atmosphere coaxially with the receiver field of view. The telescope is mounted in a fixed vertical position on the optics table that holds the transmitter and remaining receiver optics. The backscattered light collected by the telescope is collimated to facilitate transmission through a subsequent interference filter. A custom low-f-number lens is used to focus the collimated light onto a photodiode. This lens was redesigned to have a wider field of view than that described in MS. The initial lens was designed to provide a 0.54-mrad field of view (full angle) neglecting aberrations. When accounting for the blur spot size, the lens only allowed a containment of 0.48-mrad field of view within the 200-μm detector. The new lens design, used for the measurements herein, allows for a containment of a 0.56-mrad field of view on the detector. The three-element lens has a 16-mm focal length and 24-mm-diameter clear aperture.

The photodetector is a 200-μm-diameter active area InGaAs avalanche photodiode with a hybrid preamplifier (Perkin Elmer part number C30659–1550-R2A). The module is mounted on a custom amplifier board. The bandwidth of the combined detector and postam-

plifier is 50 MHz. This is a significant improvement over the system described in MS. As discussed in that paper, the amplifier response limited the instrument range resolution to ~50 m. The new combination of a hybrid preamplifier and postamplifier improves the overall range resolution to 3 m. The resulting electrical signal is digitized at up to 100 mega samples per second (MS s^{-1}) in single-channel mode or 50 MS s^{-1} in dual-channel mode.

c. Beam-steering unit

A custom 40.6-cm clear aperture BSU was designed and built at the National Center for Atmospheric Research (NCAR) Design and Fabrication Services (DFS). Figure 2 shows a solid model representation of the BSU. To protect the internal mirrors and seal the unit from the elements the BSU has a 10-mm-thick B270 glass window with an antireflection coating. The total weight of the BSU, including the mirrors described below, is 100 kg.

The BSU utilizes a 16-channel slip ring in order to transmit power to and communicate with the elevation motor. This unique design feature allows it to rotate in one azimuthal direction constantly without having to reverse to unwrap cables. This capability is important for consistent temporal atmospheric sampling when collecting full azimuthal scans. The BSU axes turn on belt-driven bearings powered by servomotors (Animatics SmartMotor). The motors are connected to a computer by serial line. All the information required for the scanning patterns is uploaded to the motor's onboard memory. This greatly reduces the amount of data passed over the serial line during operation—the motor encoder count at each laser shot is all that is required.
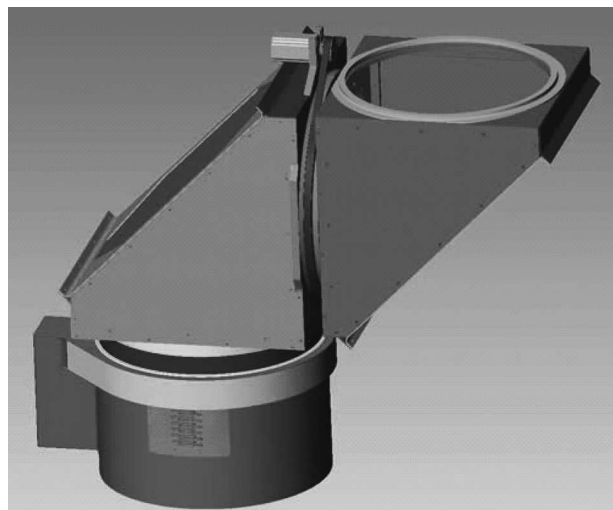
The small active area of the detector places modest requirements on the quality of the receiver optics. Optical modeling indicated that our BSU flat turning mirrors could have irregularities up to 10 waves over the full aperture. This is in contrast to Doppler lidar BSU mirrors, which typically are required to have a flatness of better than 0.1 waves over the full aperture. Given the traditional high cost of large-aperture light-weighted substrates we investigated a few different approaches for our BSU mirrors.

For a first attempt we followed Winker (1994) and Kent and Hansen (1999), who discuss a method for making lightweight and flat BSU mirrors from thin (3 mm) inexpensive glass with an aluminum honeycomb back plate. We attempted to duplicate their efforts with a 6-mm-thick (609 mm × 408 mm) mirror but were unable to achieve sufficient mirror flatness for our system requirements. As a result, we obtained a more traditional, but still moderately thin, pair of 25-mm-thick (610 mm × 432 mm) mirrors with the corners removed to reduce the total weight. The mirror substrates were Zerodur, although Pyrex should have worked equally well. The mirrors were mounted onto Hexcell aluminum back plates with a flexible adhesive. The surface sag of the composite mirrors (glass mounted to back plate) was measured with a coordinate mapping machine. The results were imported into an optical model of the receiver system to verify that the combination of the unique deviations did not produce unacceptable aberrations. The model results, shown in Fig. 3, indicate containment of >99% of all rays within a 0.24-mrad (half angle) field of view on the detector surface. This

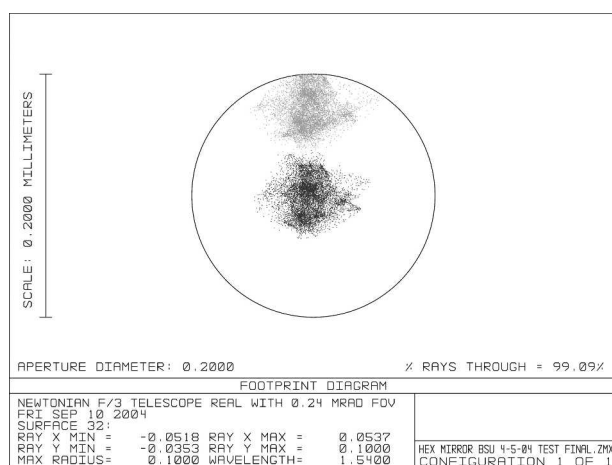FIG. 2. View of the beam-steering unit solid model.

FIG. 3. Results of the optical model calculations through the complete receiver train. Rays traced from 0.0- and 0.24-mrad field-of-view angles are shown (indicated by the black and gray data points, respectively). Calculations include sag from beam-steering-unit mirrors, which is the dominant source of aberrations.

FIG. 4. The top shipping container houses the transmitter and receiver, and the beam-steering unit is installed on its roof. The bottom gray container is an empty shipping container in order to elevate the entire system to obtain a view free from obstructions. Eye safety is imperative for operation in densely populated urban areas.

provides an acceptance angle larger than the divergence of the laser.

Each composite mirror weighs 14 kg, or 53 kg m^{-2}, whereas a solid glass substrate with a traditional aspect ratio (e.g., 1:6) would weigh 4 times more. Also, a traditional lightweight substrate (e.g., gas fusion, spin casting, etc.) would have cost nearly double; therefore, this method provided a relatively inexpensive and lightweight mirror with sufficient flatness for our application.

d. Fieldable configuration

In the spring of 2004 the transmitter, receiver, and scanner were integrated into a 6.1 m $\times$ 2.5 m $\times$ 2.5 m shipping container. The entire instrument was shipped to Washington, D.C., for its inaugural field test in early May 2004. Figure 4 shows the REAL shipping container with BSU installed on the roof during the first field test. The transmitter and receiver of the instrument take up just a small area (1.5 m $\times$ 2 m) of the interior below the BSU while the rest of the container is used as office space. The window of the BSU appears blue in color due to the antireflection coating. As one can see from the photo, scanning a non-eye-safe laser beam at low elevation angles in such a densely populated urban area would be especially dangerous given so many buildings.

3. Experimental data

The lower troposphere is rich with aerosol particles from both natural and anthropogenic sources. In particular, the atmospheric boundary layer (ABL), the lowest part of the troposphere that quickly responds to the forcings from the earth's surface, usually contains a dramatically higher concentration of particles than the "free atmosphere" above it. Therefore, most of the lidar data collected by REAL constitute an illumination of the structure of the cloud-free ABL and its internal structure. During the daytime, or under windy conditions, the ABL is typically hundreds of meters to kilometers deep, and turbulent, due to thermal convection or vertical wind shear. During the night, if sufficient cooling takes place, the ABL flow may become stable and impede turbulence.

For the following data, the instrument was located at the NCAR Foothills Laboratories in Boulder, Colorado. The site is in the northern part of the city, which lies in north-central Colorado with the Rocky Mountains immediately to the west. We typically scan slowly (4° per second) in one direction and then quickly to the

starting angle of the scan sector to increase the frequency of scans with consistent temporal sampling. Trees immediately south of the site prevent all scanning in that direction. Trees approximately 500 m to the north prevent pointing the beam any lower than a 3° elevation angle when scanning in that direction.

Thus far, we have performed only two fundamental types of scans with REAL. In both cases, the names of the scan types are inherited from the cathode-ray-tube-type displays used in early weather radars. Plan position indicator (PPI) scans are made by holding the elevation angle constant while changing the azimuth angle continuously and at a constant rate. Range–height indicator (RHI) scans are made by holding the azimuth angle constant while changing the elevation angle continuously and at a constant rate. When PPI scans are created with the elevation angle held at 0°, the scan represents a horizontal plane in the atmosphere. Typically this can only be accomplished when the lidar system is sufficiently elevated above the ground (perched on top of a tall building) or overlooking a valley. When PPI scans are collected with a nonzero elevation angle, the data lie on conic surfaces. In the examples of PPI scans presented here, the elevation angle is a relatively small 3°, and as a result the images are almost representative of horizontal planes at the bottom of the atmosphere. RHI scans always result in vertical planar cross sections of the atmosphere.

To visualize the three-dimensional structure of the atmosphere, more complex volumetric scanning strategies composed of multiple PPI- or RHI-type scans are possible. For example, the UW-VIL (Eloranta and Forrest 1992) can create RHI-volume-type scans where each RHI scan is at a slightly incremented azimuth angle in order to collect volumetric atmospheric data. However, such volumetric scans require longer amounts of time to complete at a given pulse repetition frequency transmitter. Currently, REAL operates at only 10 Hz, which is insufficient for volumetric imaging (50–100 Hz is required). We note that at 5 km the laser beam is approximately 2 m in diameter and separated by ~35 m from the previous shot when scanning at $4° \text{ s}^{-1}$.

In the data shown here, backscatter from the atmosphere was sampled at 50 MS s^{-1} to provide data points at 3-m intervals in range. The dc baseline of each average return, which is proportional to the background intensity, was subtracted based on an average of data points sampled before the laser is fired. Each lidar return is then corrected for one-over-range-squared dependence. Due to the large dynamic range the backscatter intensity is displayed in decibels. A mild smoothing filter is applied to the data in range and angle. The filter is a three-point gliding type whereby each range gate is averaged with its neighbors via a triangle weighting function (the neighboring gates are weighted at 50%). The angular smoothing uses the same type of weighting function. The data are rendered for real-time display with an OpenGL graphics system.

The following four cases demonstrate some useful applications and limitations of REAL. Each case is accompanied by an electronic animation that can be viewed in the online electronic version of this paper. The first case demonstrates the ability of the system to detect point sources of particulate matter, such as those generated by the exhaust of a locomotive. The second case demonstrates how precipitation limits the lidar's maximum range. The third case is an example of how the system can monitor the convective boundary layer depth. The last case shows strong inhomogeneity of the aerosol backscatter distribution on horizontal scales as aerosol clouds from one or more unknown sources advect through the lidar's surveillance region.

a. Locomotive exhaust: 2010–2127 UTC 25 June 2004

The selected display from the animation shown in Fig. 5a is from a sequence of near-horizontal (~3°) PPI scans collected in a 95° sector pointing toward the north. (The full animation is available online as an electronic supplement at http://dx.doi.org/10.1175/jtech1755.s1.) Each scan required approximately 30 s to collect. The system achieved a useful range of 6 km in the visibly clear Boulder atmosphere. At 2017 UTC the animation shows a plume from a diesel–electric locomotive emerging at approximately 500-m range at 340°. By 2020:45 UTC the plume appears at 1-km range directly north of the lidar site. During this period, it appears as a relatively straight line with a width of no more than approximately 50–100 m. The plume continues to appear through the scan plane as far away as 3.75 km at 2028:56 UTC. The plume advects to the northwest and either blends in completely with the background aerosols or drifts above the scan plane after 2035 UTC.

b. Rain shower: 2211–2316 UTC 25 June 2004

The next example shown in Fig. 5b is another near-horizontal PPI (elevation of 3°) over a 1-h period. (The full animation is available online as an electronic supplement at http://dx.doi.org/10.1175/jtech1755.s2.) At 2217 UTC, enhanced scattering from very light precipitation can be observed at ranges beyond 5.5 km to the northwest of the lidar site. By 2225 UTC this broad linear feature transects the image in an orientation running from southwest to northeast and attenuates the
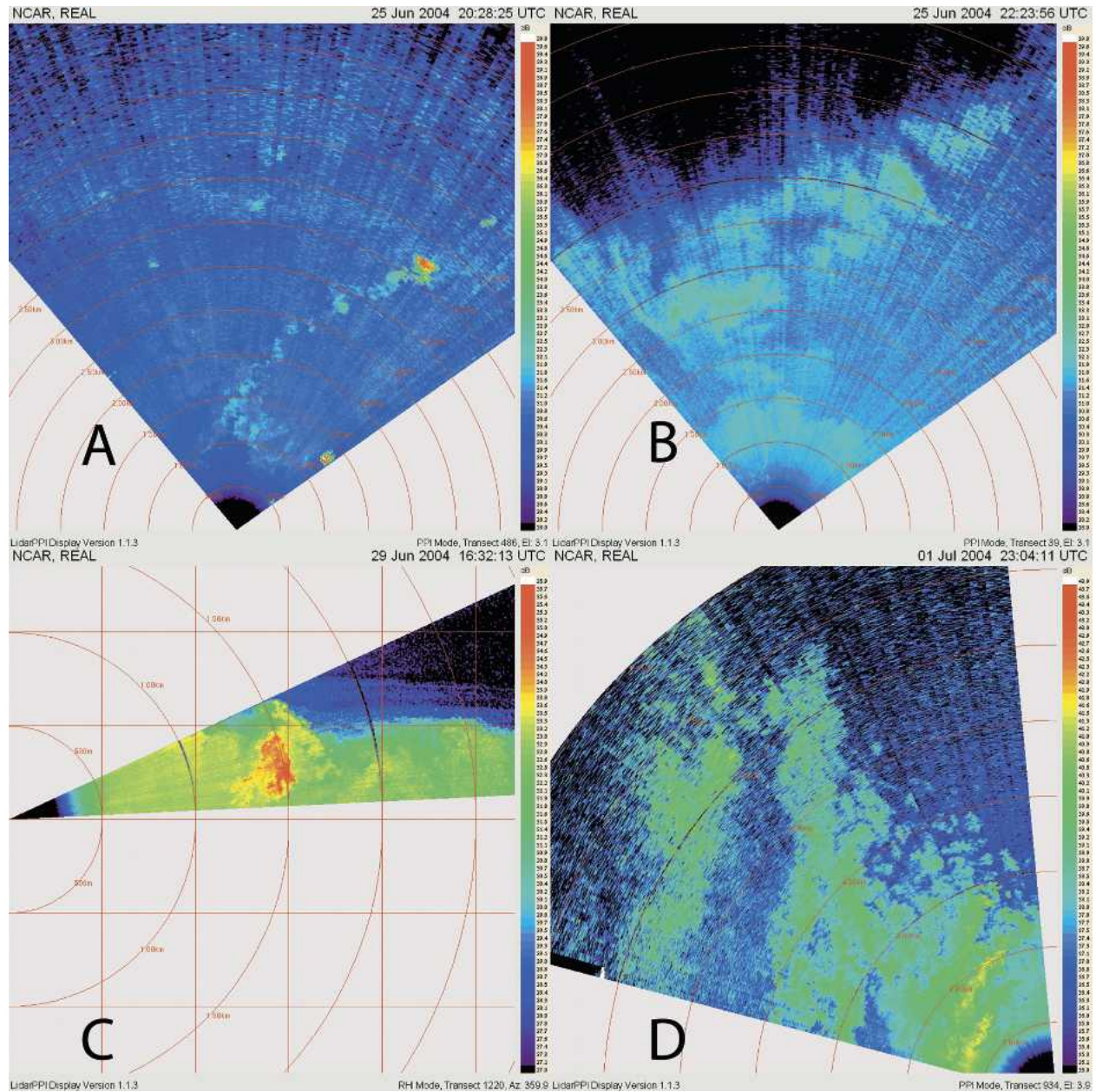
FIG. 5. (a) Image from the animation of 148 PPI scans collected in Boulder, CO, 2010–2328 UTC 25 Jun. Scan images were collected between 320° and 55° in azimuth. Range rings at every 500 m are shown. (b) Image from the animation of 125 PPI scans collected in Boulder, CO, 2211–2316 UTC 25 Jun. Scan images were collected between 320° and 55° in azimuth. Range rings at every 500 m are shown. (c) Image from the animation of 152 RHI scans collected in Boulder, CO, 1623–1728 UTC 29 Jun. Scan images were collected between 3° and 25° elevation. Grid spacing of 500 m is shown. (d) Image from the animation of 94 PPI scans collected in Boulder, CO, 2227–2304 UTC 1 Jul. Scan images were collected between 285° and 355° in azimuth. Range rings at every 1000 m are shown.

signal beyond it. At 2231:36 the precipitation has caused maximum attenuation of the lidar signal, effectively limiting useful range to approximately 1 or 2 km. However, the useful range for observing aerosol particle scattering quickly returns to more than 4 km within 10 min as the shower passes to the south of the lidar site. The band of precipitation moved more than

5.5 km over 14.5 min, giving it a mean speed of 6.3 m s^{-1}. This feature appears to move substantially faster than the aerosol structure motions observed before and after the event. A likely explanation for this is that precipitation is generated by convective clouds high above the scan plane that have a very different velocity than the air illuminated near the surface by this scan.

The lidar only sees the precipitation as it penetrates the scan surface. Therefore, the speed of the macroscopic precipitation band observed by the lidar is not indicative of the wind speed in the scan plane.

c. Convective boundary layer: 1623–1728 UTC 29 June 2004

The next example shown in Fig. 5c is an RHI that required approximately 26 s to collect. (The full animation is available online as an electronic supplement at http://dx.doi.org/10.1175/jtech1755.s3.) This image, and the animation, shows the structure of the lower 500 m of the atmosphere out to a range of 2.75 km. A turbulent boundary layer is indicated by strong aerosol scattering from the surface to approximately 500-m altitude. The boundary layer grows 200 m over the hour-long animation. A locomotive passes at 1628 UTC and 800-m range. The exhaust plume can be first observed as red against the yellow/green background. It quickly reaches the top of the boundary layer while also advecting approximately 500 m to the north. Within 7 min the plume appears to be completely mixed with the background air or it has advected east or west out of the scan plane. These data show how quickly particulate matter emitted near the surface can be lofted to the top of the convective boundary layer.

d. Unidentified aerosol clouds: 2227–2304 UTC 1 July 2004

The final example shown in Fig. 5d is a near-horizontal (4° elevation) PPI sector scan toward the northwest; an 8-km range is shown. (The full animation is available online as an electronic supplement at http://dx.doi.org/10.1175/jtech1755.s4.) The associated animation shows plumes of aerosol particles from an unknown source advecting through the scan plane. The aerosol plumes move from the northeast to the southwest of the lidar site.

4. Conclusions

NCAR's scanning REAL fills a need in the atmospheric science community for a high-pulse-energy, eye-safe, scanning aerosol backscatter lidar. Although the backscatter data do not provide measurements of particle number density or particle size distribution, the spatial images and their temporal animation provide important information about the structure and dynamics of the clear atmosphere. REAL's niche is the ability to map the spatial distribution of aerosols in the visually clear atmosphere and provide animations of those images, as we have shown here. These data are of interest particularly to atmospheric researchers who must have

a complete picture of atmospheric structure for their analysis [see Mayor et al. (2003) for an example of the application of this type of data]. An instrument like REAL is best used simultaneously with other instruments, such as radiosondes, in situ weather sensors, and radars, in order to obtain the most complete view of the atmosphere.

An important requirement that must be met in order to make high-quality lidar animations is the ability to generate the individual scan images (frames) at time intervals substantially less than the correlation time of the atmosphere. In addition to the horizontal translation due to the mean wind, turbulence is constantly acting to change the shape of the aerosol distribution structure. In the atmospheric boundary layer, the correlation time due to turbulence is usually on the order of 1 min or more, although it varies with altitude, boundary layer depth, and turbulence intensity. REAL is currently able to make PPI sector images with sufficient angular resolution and aerial coverage at a rate of about 1 frame per 20 or 30 s. In the future, a higher-pulse-repetition-frequency laser will allow us to collect either broader scans in the same amount of time or scans equally as wide as now but in substantially less time. Broader scans will allow atmospheric researchers to sense a larger area of the atmosphere, while faster scans will allow higher angular resolution and temporal sampling.

Eye safety is imperative for routine operation of such a device, especially in densely populated urban areas or near research aircraft. In the future, we plan to increase the pulse energy and repetition rate, reduce the size of the entire instrument, and work toward continuous and unattended operation. We will also add a second channel to the receiver and measure depolarization of the backscattered light.

REFERENCES

Eloranta, E. W., and D. K. Forrest, 1992: Volume-imaging lidar observations of the convective structure surrounding the flight path of a flux-measuring aircraft. *J. Geophys. Res.,* **97,** 18 383–18 393.

——, J. M. King, and J. A. Weinman, 1975: The determination of

wind speeds in the boundary layer by monostatic lidar. *J. Appl. Meteor.,* **14,** 1485–1489.

Kent, G. S., and G. M. Hansen, 1999: Scanning lidar with a coupled radar safety system. *Appl. Opt.,* **38,** 6383–6387.

Kunkel, K. E., E. W. Eloranta, and S. T. Shipley, 1977: Lidar observations of the convective boundary layer. *J. Appl. Meteor.,* **16,** 1306–1311.

Laser Institute of America, 2000: Standard for the safe use of lasers. Tech. Rep. ANSI Z136.1. [Available from American National Standards Institute, 1819 L St., NW, Suite 600, Washington, DC 20036.]

Mayor, S. D., and S. M. Spuler, 2004: Raman-shifted eye-safe aerosol lidar. *Appl. Opt.,* **43,** 3915–3924.

——, G. J. Tripoli, and E. W. Eloranta, 2003: Evaluating large-eddy simulations using volume imaging lidar data. *Mon. Wea. Rev.,* **131,** 1428–1453.

Winker, D., 1994: Fabrication and testing of large steering mirrors for a scanning lidar. *Appl. Opt.,* **33,** 5712–5714.